Classification of Synoptic Patterns with Mesoscale Mechanisms for Downslope Windstorms in Korea using the Self-Organizing Map

Yewon Shin[1], Jung-Hoon Kim[1]*, Hye-Yeong Chun[2], Wook Jang[3], and Seok-Woo Son[1]

[1]School of Earth and Environmental Sciences, Seoul National University, Seoul, South Korea.

[2]Department of Atmospheric Sciences, Yonsei University, Seoul, South Korea.

[3]Korea Meteorological Institute, Seoul, South Korea.

Corresponding author: Prof. Jung-Hoon Kim (jhkim99@snu.ac.kr)

Key Points:

- Using the Self-Organizing Map algorithm, synoptic patterns for downslope windstorms in Korea are classified into three representative types.
- Different features for three types are found in the synoptic fields, the Föhn effect, and the characteristics of upstream vertical profiles.
- Dominant mesoscale mechanisms of the downslope windstorms are different significantly under the three classified synoptic patterns.

Abstract

Downslope windstorms are responsible for wildfires, wind gusts, and turbulence in the lee side of the Taebaek Mountains, called Yeongdong region (YD) in Korea. We classified the synoptic conditions of the windstorms in the YD using a Self-Organizing Map (SOM). For the windstorm events from 1979 to 2019, sea level pressure anomalies were used to train the SOM. It was found that the synoptic patterns could be classified into three representative types: 1) the south high and north low pattern in spring, 2) the west high and east low pattern in winter, and 3) the strong low-pressure system passing the northern part of Korea. At the 850 hPa level, prevailing southwesterly (nortwesterly) flow with warm (cold) advection was dominant in Type 1 (2), and Type 3 presented a well-developed baroclinic system of cyclone. Adiabatic warming by downslope windstorm is the strongest in Type 1, which is likely to have a huge impact on the spread of wildfires. Three mesoscale generation mechanisms were examined under different synoptic patterns. Hydraulic jump theory was dominant for the windstorms in Type 2 due to upstream flows with moderate Froude numbers and inversion layers. The partial reflection of mountain waves was found in all types but more frequent in Type 1 than others. Downslope windstorms with wave breaking at critical levels mostly occurred in Type 1. This objective classification of weather patterns responsible for downslope windstorm in the YD is useful for better prediction and future projection of this event with climate change.

1 Introduction

Downslope windstorms (DWs), which occur when the atmospheric flow over a mountain accelerates in the mountain's lee, are responsible for wind gusts, turbulence, and rapid spread of wildfires. They are observed in many mountainous regions in the world, including the Rocky Mountains in the United States (Lilly 1978), the Alps in Europe (Hoinka 1985), and the Andes Mountains in South America (Seluchi et al. 2003).

Three representative generation mechanisms of the DW have been suggested in the previous studies. Based on the theoretical analysis of Long (1953) on two-dimensional stratified flow over an isolated barrier, Long (1954) proposed the hydraulic jump theory, which suggests that a subcritical upstream flow is changed to a supercritical flow when it goes over a mountain range. An accelerated flow generates severe winds and turbulent jump motion in the lee of a mountain. This transition of flow occurs if the Froude number (Fr) is subcritical but not too small and when the assumed rigid upper surface of the fluid is not too deep compared with the height of the mountain (Long 1954; Houghton and Kasahara 1968). A hydraulic jump occurs even if the rigid lid preventing energy from propagating upward does not exist and the fluid is continuously stratified (Durran 1986). Lin and Wang (1996) divided the flow regimes of a two-dimensional stratified flow over an isolated mountain ridge and reported that a significant lee jump occurred and that severe DW was generated if the Fr was between 0.6 and 1.12. Klemp and Lilly (1975) suggested that vertically propagating mountain waves can be partially reflected at the level of sudden changes in atmospheric stability and vertical wavenumber. The optimal superposition of upward- and downward-propagating waves can amplify the horizontal wind speed near the surface by transporting energy downward. This mechanism, which was developed from the linear theory and the simple mult-layer structure of atmosphere, can be applied in cases when hydraulic jumps cannot explain phenomena due to their restrictive assumptions. Mountain wave breaking at a critical level can cause DW (Clark and Peltier 1984). If upward-propagating stationary waves meet the reversed background zonal wind ($U = 0$) or wave-induced critical

level with a local Richardson number (Ri) below 0.25, these waves are not absorbed but instead strongly reflected. Additionally, if the vertical wavelength is equal to $n + \frac{3}{4}$ $(n = 0, 1, 2, \cdots)$ of the critical level height, the constructive resonance of waves can amplify nonlinear wave breaking above the mountains and can generate intense DWs.

In Korea, the Taebaek Mountains (TM) are elongated from north to south in the eastern side of Korea, and their top heights are approximately z = 1000–1500 m. Figure 1 shows the topography of Korea, with the locations of the TM and cities on its lee side; this is called the Yeongdong region (YD). In this region, the lee slope is so steep that DW events frequently occur in the springtime and the wintertime of Korea and have been responsible for historical wildfires. DW also caused structural damage, cancellations, and delays of the ski jump and biathlon competitions on 14–15 Feb 2018 during the 2018 PyeongChang Winter Olympic Games. Many previous studies have reported that a south high and north low synoptic-scale sea level pressure (SLP) pattern, accompanied by warm advection and an inversion layer near the top of the mountains, is often observed when DW occurs in the springtime in the YD (Kim and Chung 2006; Jang and Chun 2010; Cho et al. 2015; Lee et al. 2020). Regarding the generation mechanisms of DW events in this region, Kim and Chung (2006), and Jang and Chun (2010) examined the hydraulic jump theory and wave breaking for a DW event on 5 April 2005 when a historical wildfire occurred. Additionally, Jang and Chun (2008) considered the three abovementioned mechanisms using 30 years of upstream sounding data (1976–2005) and revealed that partial reflection, hydraulic jump, and critical level reflection (in that order) generated the most DW events in the springtime.

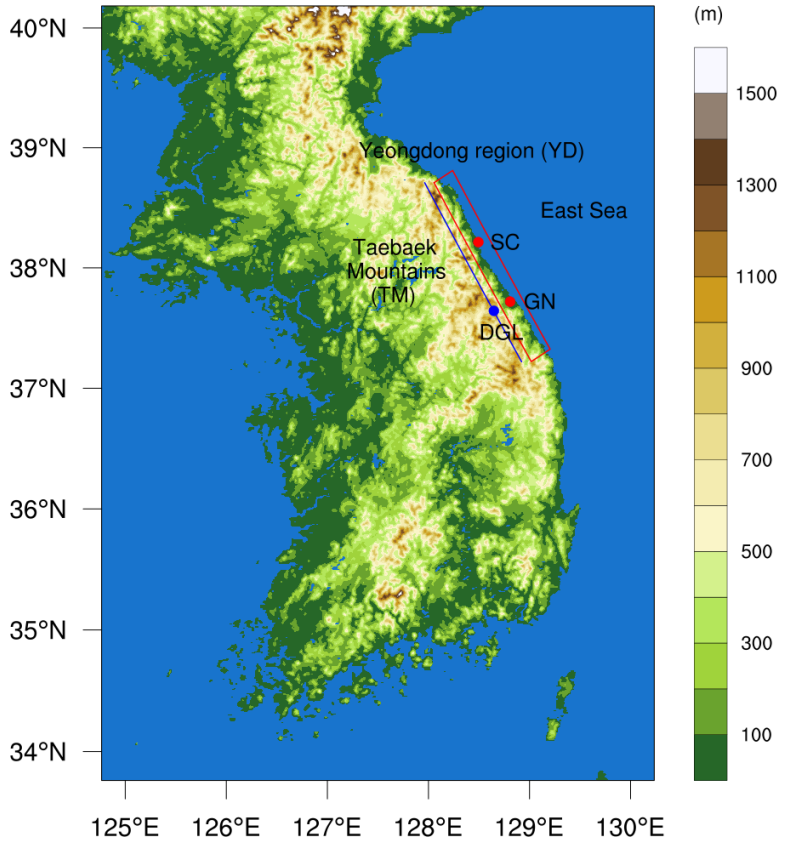

Figure 1. Topography of Korea (shading). Taebaek Mountains (TM) and Yeongdong region (YD) are indicated as a blue line and a red box, respectively. Sokcho (SC) and Gangneung (GN) (two cities in the YD) are depicted as red dots, and Daegwallyeong (DGL) (a town on the TM) is depicted as a blue dot.

The authors of this study aimed to classify the underlying synoptic SLP patterns responsible for the DWs in the YD in Korea using a self-organizing map (SOM). Though the typical SLP pattern of the DWs is south high and north low in the springtime, there must be other patterns because DW events occur not only in the spring, but also in the late fall and winter (Cho et al. 2015). Several studies have classified weather patterns using clustering algorithms. One method is to characterize the meteorological patterns in the climatological data and investigate the occurrence of extreme weather such as heat waves and heavy rainfall in each pattern (Loikith et al. 2017; Glisan et al. 2016). Cho et al. (2019) classified representative weather patterns in the East Asia region using the k-means clustering algorithm and identified the patterns related to extreme weather in Korea. They also stated that classifying the weather patterns of the specific severe weather phenomena is necessary to gain further insights for better predictions. Jo et al. (2020) classified localized heavy rainfall events in the summertime in South Korea using the k-means clustering and SOM algorithms, and Nguyen-Le and Yamada (2019) also classified synoptic patterns responsible for summertime heavy rainfall over Northwestern Thailand using the two algorithms. Furthermore, many studies have suggested methods to statistically evaluate the forecast skill of patterns recognized by the clustering algorithms, as well as the significant improvements in skill score with this approach (Neal et al. 2016; Ohba et al. 2016; Nguyen-Le and Yamada 2019).

In this study, we classified the SLP patterns of DW events using the SOM algorithm and seasonal variability and tropospheric synoptic fields. In addition, we examined the characteristics of the meteorological variables affecting surface environment in the YD and background flows determining the dominant mesoscale mechanisms for the DW events in each pattern. The remainder of this paper is constructed as follows. The data and methods are in Section 2, which explains the definition of the DW events and brief description of the SOM algorithm. Section 3 presents the characteristics of the selected DW events. The SLP patterns classified with the SOM, along with corresponding seasonal variability and synoptic-scale composite maps at the 850 hPa level, are discussed in Section 4. Section 5 shows the different adiabatic warming effect with temporal changes in the surface temperature in each pattern. In section 6, the dominant mesoscale mechanisms of DWs with analyses of background flows under the different synoptic patterns are addressed. Finally, the conclusion is provided in Section 7.

2 Data and Methods

2.1 Data

We used the daily maximum instantaneous wind speed obtained from automated surface observing system (ASOS) data measured at Sokcho (SC) and Gangneung (GN) to define the DW events. Hourly surface temperature from the ASOS data measured at GN and Daegwallyeong (DGL) were used to investigate the warming effect of DW. The locations of the surface weather stations at SC, GN, and DGL are indicated in Fig. 1, showing that SC and GN are on the lee side of the TM, and DGL is at the top of the TM and to the west of GN. The SLP and 850 hPa

variables (geopotential height, temperature, and horizontal wind speed) obtained from the National Centers for Environmental Prediction–Department of Energy (NCEP–DOE) Reanalysis 2 data were used to identify the synoptic-scale patterns of the DWs. This dataset is an improved version of the National Centers for Environmental Prediction–National Center for Atmospheric Research (NCEP–NCAR) reanalysis data with fixed known errors and updated parameterizations. It provides 6 hourly (00, 06, 12, and 18 UTC) global data from 1979 to the present with 2.5° × 2.5° horizontal grid spacing. In addition, the fifth-generation of the ECMWF reanalysis (ERA5) hourly data on pressure levels were used to examine the mesoscale generation mechanisms of the DW events. Their horizontal grid spacing is 0.25° × 0.25°, and their vertical layer spacing is 50 hPa for the 750–250 hPa levels and 25 hPa for the 1000–750 and 250–100 hPa levels. We used different reanalysis data with different horizontal resolutions for synoptic-scale and mesoscale analyses for two reasons. First, we used the SOM to classify the underlying synoptic-scale patterns with the relatively coarse resolution of reanalysis data because the SOM is sometimes sensitive to local-scale features, especially near mountainous areas. Second, when we further examined the generation mechanisms of the DWs under certain synoptic patterns, it was necessary to look at more detailed mesoscale features from the ERA5 data across the TM. Finally, all datasets mentioned here were used for 41 years from 1979 to 2019.

2.2 Identifying Downslope Windstorm Events

We defined the DW events when the daily maximum instantaneous wind speed exceeded 20 m s^{-1} at SC or GN, which are two cities in the YD (Fig. 1). This value was chosen based on the criterion for issuing the wind advisory by the Korea Meteorological Administration (KMA). Since those data were provided once a day but SLP data were provided four times a day, we divided the event into two separate events in a case that the times when the maximum wind speed was measured at the SC and GN were not close within the same day. To only include windstorms in the YD generated by flows passing over the TM, we excluded cases with wind directions between 0 and 180 degrees, which means that the wind was not from the west. We also excluded cases affected by a typhoon that originally developed from the Northwest Pacific Ocean, because it caused strong gusty winds near surface regardless of DW generation. As a result, we collected 668 cases in total and 600 days with the DW events for 41 years.

2.3 Self-Organizing Map (SOM)

SOM is a nonlinearly projecting mapping algorithm introduced by Kohonen (1995) that is highly related to classical vector quantization (Kohonen 2013). SOM measures Euclidean distances between each input datum and each initialized node vector. Then, SOM assigns each input datum to the best-matching unit among the nodes, which has the smallest distance from the data. Then, it updates the node vectors of the best-matching and adjacent units toward the input data to minimize the mean distance. By iterating this process and training SOM, it converges to an optimal result. SOM is a kind of unsupervised neural network algorithm, so it can even be used in cases when there is no expected result from input data that is useful for setting up objective classifications or patterns for weather events (Ohba et al. 2016; Loikith et al. 2017; Nguyen-Le and Yamada 2019). SOM usually conducts clustering analysis by dimension reduction, representing high-dimensional input data as a few two-dimensional data. It can additionally be used to extract some predicted features from all data (Liu et al. 2006). SOM is different than other mapping algorithms because SOM preserves topography. In SOM, nodes are

arranged in a specified grid on a map. Their topographical relationship is preserved by updating the vectors of the best-matching and adjacent units together, which are related each other according to neighborhood functions. Through this process, similar data are associated with adjacent nodes while dissimilar data are located far away (Kohonen 2013). Therefore, data become spatially and globally ordered.

In this study, SLP anomalies from over 41 years (1979–2019) were used as an input data to train the SOM. Though many studies have used several meteorological variables together (multivariate input data) for identifying weather patterns (Ohba et al. 2016; Loikith et al. 2017; Nguyen-Le and Yamada 2019), we only used SLP anomalies (univariate input data), which show the representative synoptic-scale patterns for DW in the YD revealed in the previous studies (Kim and Chung 2006; Jang and Chun 2010; Cho et al. 2015; Lee et al. 2020). The classification results of multivariate input data (SLP and 850 hPa temperature anomalies) also showed similar patterns to the test with only SLP anomalies, so we used the classified SLP patterns from the SOM results with a univariate input and then investigated the composite maps of the synoptic-scale fields at the 850 hPa level corresponding to each cluster.

The domain of the input data was determined as 20–60° N and 100–150° E to focus on the East Asian region centered on the Korean Peninsula, following the work of Cho et al. (2019), who showed that this data domain explains better the variance in daily mean surface temperature driven by synoptic flow in Korea for all seasons compared to results with a larger domain (10–70° N and 80–160° E). A batch training algorithm was adopted because it is safer and faster than a stepwise recursive algorithm (Kohonen 2013). The SOM training algorithm contains some tuning parameters such as lattice structure, map shape, initializing node vector methods, and neighborhood functions. We used a rectangular lattice of the sheet shape, linear initialization, and Epanechikov neighborhood function, as recommended by Liu et al. (2006).

The classification results of the SOM are highly dependent on the number of clusters. A large array with more clusters can show the detailed structures of a pattern, but there should be a sufficient number of cases (approximately 50) in each cluster for statistical accuracy (Kohonen 2013). To determine the number of clusters while optimally classifying the SLP patterns for the DW events in the YD, we calculated the ECV (explained cluster variance), which is defined as (Philipp et al. 2007)

$$\mathrm{ECV} = 1 - \frac{\mathrm{WSS}}{\mathrm{TSS}}, \quad (1)$$

where WSS is the "within cluster sum of squares of deviations" and TSS is the "total cluster sum of squares". WSS measures the dissimilarity between data in a cluster, and it is calculated as (Philipp et al. 2007):

$$\mathrm{WSS} = \sum_{j=1}^{k} \sum_{i \in C_j} D(X_i, \bar{X}_j)^2, \quad (2)$$

where k is the number of clusters, C_j is a set of each cluster, X_i is each input datum and $\bar{X}_j$ is each cluster centroid that can be considered an average of the data in a cluster. Euclidean distance between each input datum and each cluster centroid is calculated as follows:

$$D\left(X_i, \bar{X}_j\right) = \left[\sum_{l=1}^{m} \left(X_{il} - \bar{X}_{jl}\right)^2\right]^{1/2}. \quad (3)$$

TSS is equal to WSS when $k = 1$ (Philipp et al. 2007). The ECV varies between 0 and 1, and it is maximized when the centroids fully explain the data in each cluster. Therefore, the ECV

measures the ability of cluster centroids to represent and explain the data in each cluster. Figure 2a, b show the ECV and the slope of the ECV curve, respectively. A rapidly increasing ECV was found to be saturated with an increasing number of clusters. Additionally, we checked the topographic error (TE) of the SOM. The TE is a ratio of input data in which the first and second best-matching units (which have the first and second smallest Euclidean distances from the data, respectively) are not located in the adjacent nodes. If the TE is relatively large, then the SOM result is not likely to be spatially ordered and optimally classified. In Fig. 2c, the rapidly increasing TE can be seen as saturated by the large number of clusters, as with ECV but with more fluctuations, and the TE sometimes has a local minimum in small numbers of clusters, such as eight with two rows and twelve with three rows. Therefore, we chose the total number of clusters to be eight (shown as a dashed vertical line in Fig. 2a–c), with two rows and four columns, when the saturation of ECV begins with the significantly decreasing slope of the ECV curve below 0.02 (shown as an upper solid horizontal line in Fig. 2b), and the TE has a local minimum of 0.0943. These choices ensured both the ability to explain the included data within clusters and the robust topographic relationship of classification result (Kohonen 1995; Kiviluoto 1996), which suggests that the patterns were balanced enough to show a sufficient range of essential patterns (Nguyen-Le and Yamada 2019).

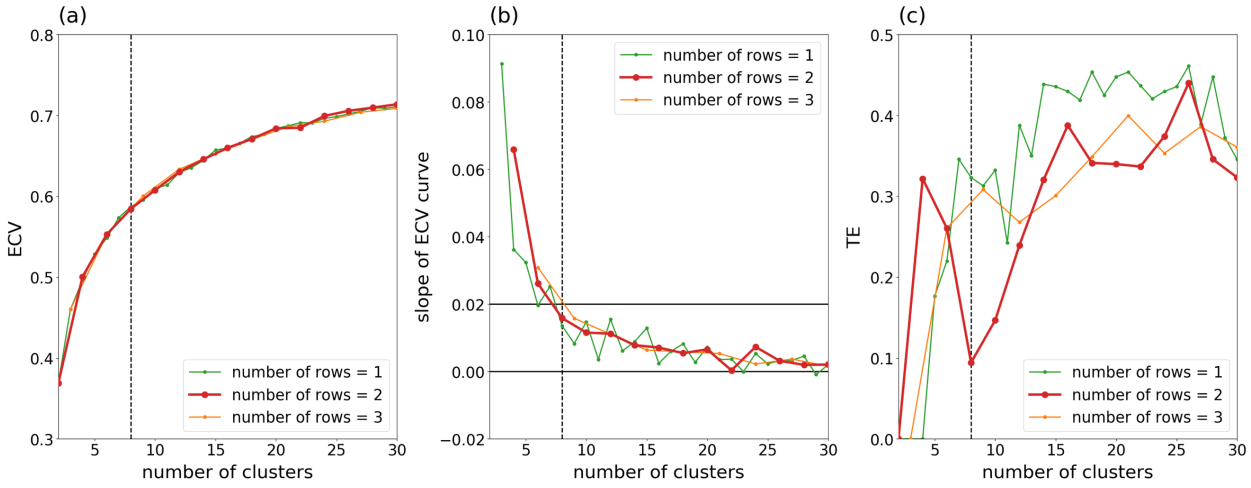

Figure 2. (a) Explained cluster variance (ECV), (b) the slope of ECV curve, and (c) topographic error (TE) with the increasing number of clusters for the different number of rows. To determine the optimal number of clusters, two black horizontal solid lines of zero and the threshold of the slope (0.02) are drawn in Fig. 2b. The optimal number of clusters, eight, is indicated as a black vertical dashed line in Fig. 2a–c.

3 Characteristics of Downslope Windstorm Events

This section explains the overall characteristics of DW events for 41 years from 1979 to 2019. Figure 3a shows the time series of the daily maximum instantaneous wind speeds with their annual mean over the research period at SC and GN on the lee side of the TM. It is likely that the annual mean speeds decreased over the whole period at both sites, although they slightly increased in the early 2000s and decreased again in the 2010s. It was also found that the frequency of DW events had a negative trend as the number of the daily maximum instantaneous wind speeds exceeding 20 m s^{-1} (upper horizontal black dashed lines in Fig. 3a) gradually

decreased. Figure 3b indicates the number of days with DW events in each year. In this figure, total occurrence means the number of days with DW events in each year at SC or GN. The frequency of DW events significantly decreased, which is revealed from fewer days of DWs per year at both sites after 1990 than before 1990. The frequency of DWs slightly increased in the early 2000s and decreased again in the 2010s (Fig. 3b), which is consistent with the trend of the daily maximum instantaneous wind speeds in Fig. 3a.

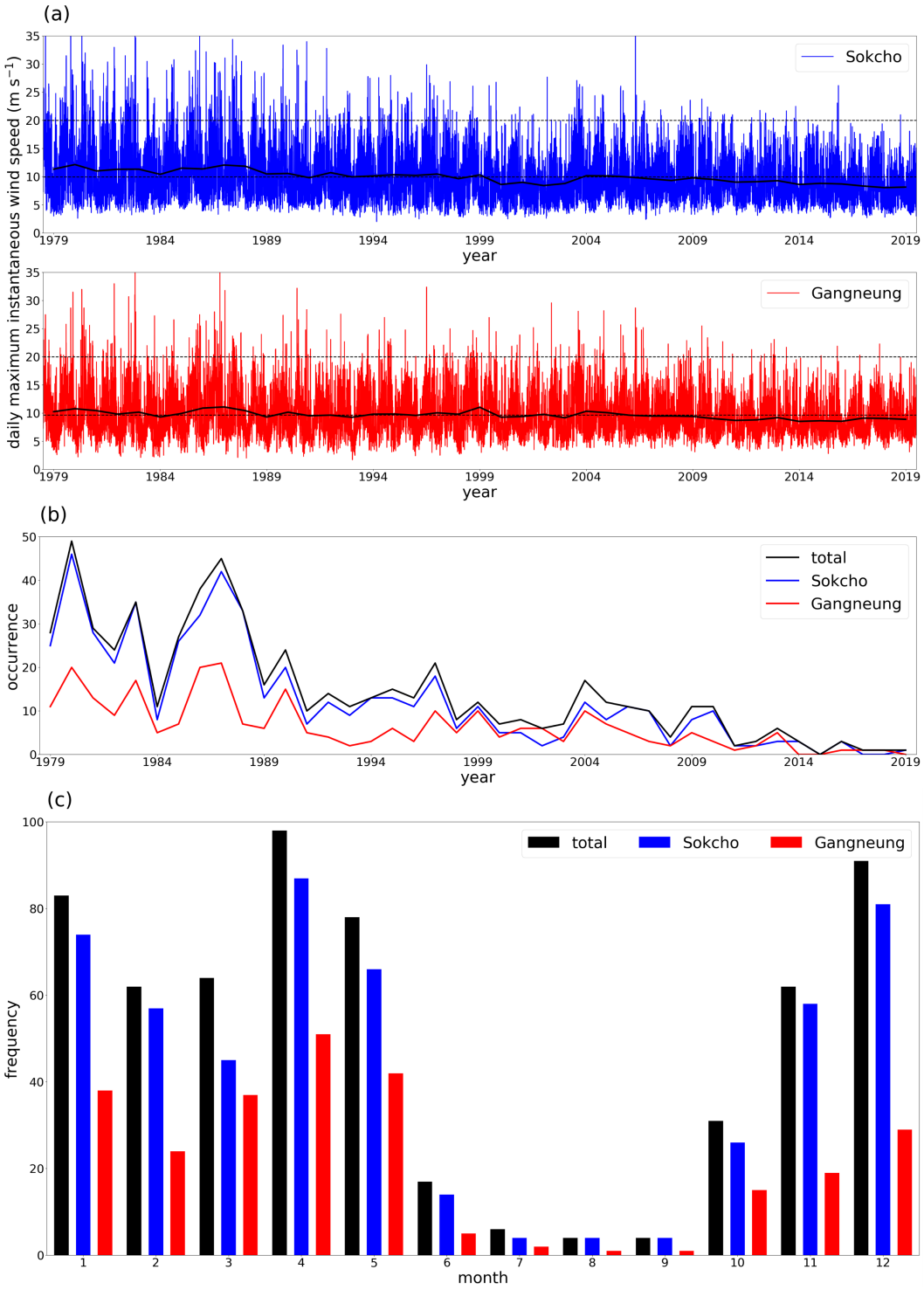

253 **Figure 3**. (a) The time series of the daily maximum instantaneous wind speeds at SC (top) and
254 GN (bottom). The black solid lines indicate the annual mean daily maximum instantaneous wind
255 speeds. The upper black dashed lines indicate 20 m s^{-1} (the threshold of DWs in this study), and
256 the lower ones indicate the mean daily maximum instantaneous wind speed over 41 years. (b)
257 The number of days with downslope windstorm (DW) events in each year. (c) The monthly
258 distribution of the whole DW events.

259

260 This long-term DW trend in the YD is similar to those of reports from previous studies.
261 Decreases in surface wind speeds, namely stilling, have been found to be significant for a few
262 decades before 2010 on continental areas in the Northern Hemisphere (NH) partly due to
263 atmospheric circulations (Vautard et al. 2010; Zeng et al. 2019) and/or increase in surface
264 roughness (Vautard et al. 2010). However, surface wind speeds have recovered over the last
265 couple decades in global areas (Zeng et al. 2019) including South Korea (Kim and Paik 2015)
266 due to changes in atmospheric circulations. Though the frequency of DWs decreased in the
267 2010s, the negative trend before 2000 and the positive trend during the 2000s reported in this
268 study are consistent with previous studies for wind stilling in NH. Additionally, it has been found
269 that changes in surface wind speeds are more significant for strong winds (Vautard et al. 2010),
270 and the annual mean wind speeds at coastal stations in South Korea have been found to more
271 rapidly decrease before the recovery of stilling than those at inland stations (Kim and Paik 2015).
272 These facts support the significant decline in instantaneous wind speeds at the two coastal
273 stations in this study. However, it is not clear whether gusty winds or DW events in the YD will
274 increase in the future. The overall decreasing trend over the past 41 years does not ensure a
275 continuous decrease in DW events in the future due to the slight increase in the 2000s, and these
276 events will be affected by changes in large-scale atmospheric circulations as revealed in previous
277 studies. Therefore, finding representative patterns for the DW proposed in this study is
278 neccessary to understand underlying large-scale flow patterns with downscaling mesoscale
279 processes for DW events, which may be eventually useful in projecting these patterns for future
280 climate scenarios.

281 The time series of the maximum instantaneous wind speeds in Fig. 3a are likely to have
282 oscillatory patterns with the seasons. To investigate the seasonal variability of DW events, the
283 monthly frequency of the DW events is shown in Fig. 3c. The monthly distribution of the DW
284 events shows two peaks in April and December. Consistent with previous studies of DWs in the
285 YD, they most frequently occurred in the springtime. We found the wintertime to have the
286 second most frequent DW occurrence and the number of DWs in December to be similar to that
287 in April. Wintertime DWs in the YD have rarely been addressed in the literature despite their
288 high frequency, but Cho et al. (2015) mentioned that DWs in the YD also occurred in the fall and
289 winter from 2005 to 2010. It was expected that the patterns of DWs in the springtime and the
290 wintertime would be different, which is addressed in Section 4.

291

292 **4 Classified Synoptic Patterns**

293 4.1 SLP Patterns

294 Figure 4 shows the classified synoptic-scale anomalous SLP patterns for the DW events
295 of the eight clusters based on the SOM. The patterns show the averaged SLP anomalies within

each cluster, which are identical to the cluster centroids. The numbers of events in each cluster displayed at the top of each plot show that the events were evenly distributed to the individual clusters ranging from 62 to 102, so each cluster centroid is statistically accurate with a sufficient number of data (Kohonen 2013). We also conducted a Student's t-test to ensure that the anomalous SLP patterns for the DW events were unique and robust compared with the climatological SLP anomalies. For all eight SLP patterns, statistically significant areas with *p*-values below 0.01 are depicted as black dots in Fig. 4; synoptic-scale high- and low-pressure systems in all patterns were statistically significant, with the confidence levels higher than 99%.

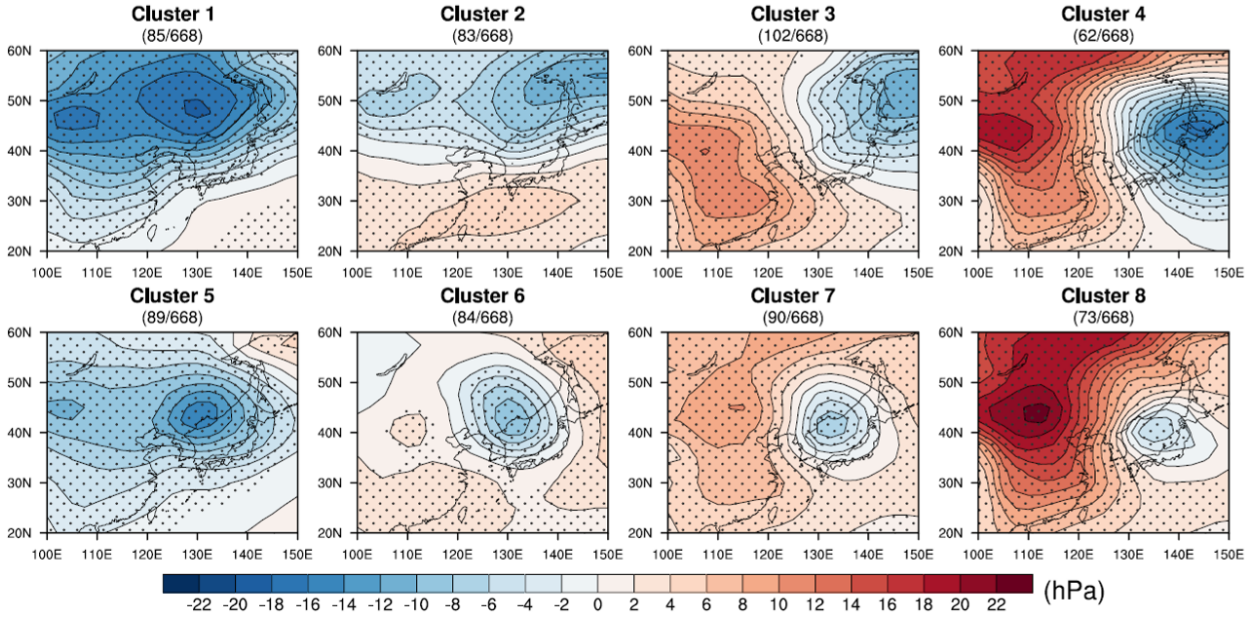

Figure 4. Synoptic-scale sea level pressure (SLP) anomaly patterns of dowslope windstorms (DWs) for eight clusters classified by the Self-Organizing Map (SOM) averaged within each cluster; 99% of statistically confident areas below the *p*-values 0.01 are depicted as black dots.

The SLP patterns in each cluster were found to be spatially ordered in this node arrangement. In the patterns on the left side of the node array, high- and low-pressure systems were found to be in the north and south of the Korean Peninsula, respectively. On the other hand, in the patterns on the right side of the node array, high- and low-pressure systems were found to be located in the west and east of the Korean Peninsula, respectively. Additionally, the low-pressure systems were found to be more localized and located closer to the northern part of the East Sea of Korea in the patterns at the bottom panel than those at the top panel. All patterns were found to have very dense isobars across the Korean Peninsula, implying that strong horizontal pressure gradients are dominant and favorable for strong background winds there.

Those eight classified patterns could be grouped into three representative types according to the locations of high- and low-pressure systems relative to the Korean Peninsula. Clusters 1, 2, and 5 were found to correspond to Type 1, the south high and north low pattern; clusters 3, 4, and 8 were found to correspond to Type 2, the west high and east low pattern; and clusters 6 and 7 were found to correspond to Type 3, the strong low pressure system passing in the northern part of Korea. There were differences between clusters in each group, but they showed common relative locations of high and low SLP anomalies. In Type 1, clusters 1 and 5 were found to show

less significant high-pressure systems than cluster 2, but relatively high and low anomalies are in the south and north of the Korean Peninsula respectively. Similarly, cluster 3 was found to have a weaker high-pressure system and less dense isobars than clusters 4 and 8 in Type 2, but high and low anomalies are in the west and east of the Korean Peninsula respectively. Finally, in Type 3, clusters 6 and 7 showed similar patterns to clusters 5 and 8, respectively, due to the topographical relationship of nodes, but they were only found to have highly significant cyclones in the northern part of the East Sea of Korea.

4.2 Monthly Distribution

Since synoptic fields in the mid-latitudes are highly dependent on seasons, we investigated the seasonal variability of each pattern by counting the number of events in each month. Figure 5 shows monthly frequency bar charts in each cluster. The patterns in the left panel were found to be more frequent in the springtime from April to May, and those in the right panel were found to occur more often in the wintertime from December to February. These results are consistent with the spatial order of clusters and show that the classified SLP patterns can be divided into springtime and wintertime DWs.

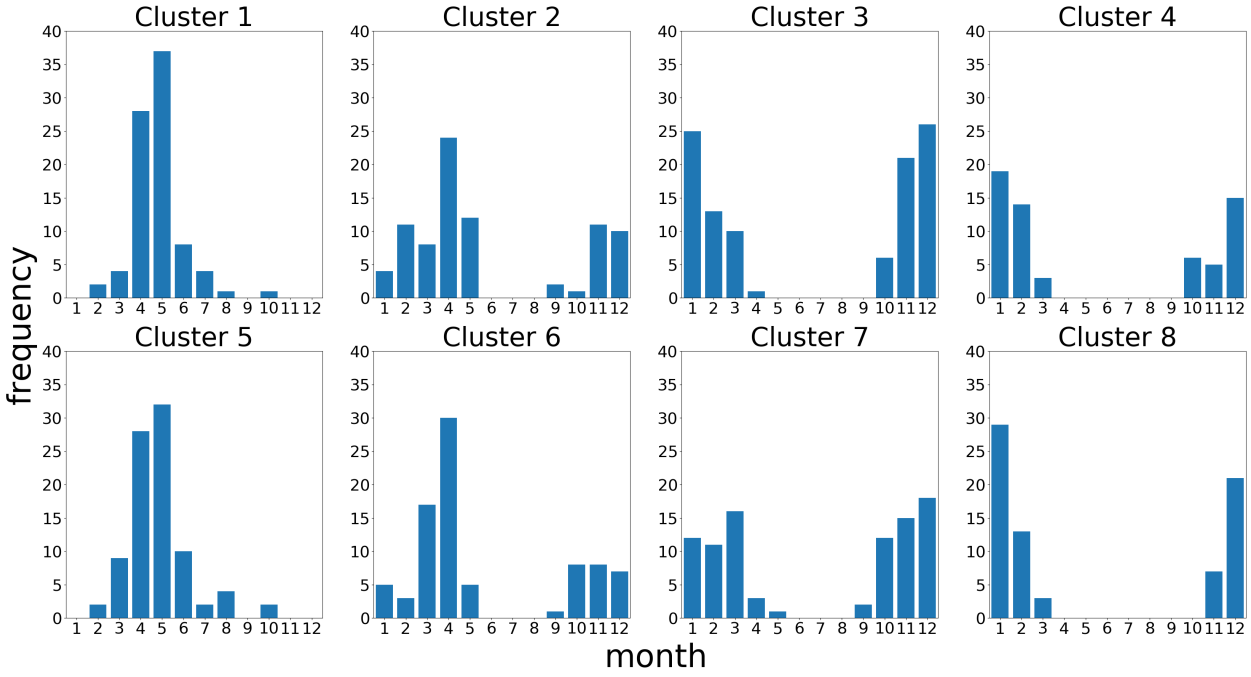

Figure 5. The monthly distribution of downslope windstorm (DW) events in each cluster classified by SOM.

The occurrence of Type 1 (clusters 1, 2, and 5 in the left panel in Fig. 5) was found to be dominant in the springtime. In this pattern, a high-pressure system moves from Central or Southern China to the Northwest Pacific Ocean and a low-pressure system moving eastward from Northern China is located in the north or northeast of the Korean Peninsula. Accordingly, there are dense isobars across the Korean peninsula between the high- and low-pressure systems. This south high and north low pattern has often been mentioned as a typical synoptic SLP pattern

that causes DWs in the YD in previous studies (Kim and Chung 2006; Jang and Chun 2010; Lee et al. 2020).

Type 2 (clusters 3, 4, and 8 in the right panel in Fig. 5) was found to mostly occur in the wintertime. In this pattern, a strong high-pressure system (Siberian high) formed by accumulated cold air masses on the Eurasian continent during the winter is extended to eastern China and Korea, and a low-pressure system develops in the East Sea or moves eastward to Hokkaido, Japan (Aleutian low). These systems eventually form dense isobars between the high on the left and the low on the right, consequently providing strong background and gusty surface winds across the Korean Peninsula (Cho et al. 2015).

Type 3 (clusters 6 and 7 in the bottom panel in Fig. 5) was observed in both spring and winter. However, cluster 6 was found to most frequently occur in March and April, and cluster 7 was found to mostly occur from October to March, reflecting similarity with the spatially close patterns in the SOM node arrangement. Close isobars are formed near the low-pressure system, rather than the relatively weak high-pressure system. This type may have a surface front that can cause strong wind with precipitation in upstream.

4.3 850 hPa Synoptic Fields

Figure 6 shows the corresponding synoptic fields at the 850 hPa level within each cluster. Anomalies of temperature, geopotential height, and horizontal wind speed were calculated by subtracting monthly averaged data from each set and then by averaging the result within each cluster. This analysis was carried out to compare the fields between clusters with different seasons and to identify relatively warm and cold areas within each cluster. In Type 1 (clusters 1, 2, and 5), the prevailing southwesterly flow with warm advection was dominant over the Korean Peninsula. This warm air, which was found to follow the boundary of the high-pressure system from Southern China to the Northwest Pacific Ocean in the spring, flows into Korea with the southwesterly winds. Meanwhile, Type 2 (clusters 3, 4 and 8) shows prevailing northwesterly flow with cold advection over the Korean Peninsula in accordance with the expansion of Siberian high. This cold air mass is from the eastern Eurasian continent, and it moves to Korea when the high-pressure system extends and produces strong northwesterly inflow. Those two patterns can be distinguished from the opposite synoptic thermal characteristics. In Type 3, the areas of cold and warm advection could be identified well in the back and front of the cyclonic anomaly, respectively. The cyclonic circulation was found to be so significant that the low-pressure system centered at the northeastern side of the Korean peninsula could be considered a well-developed, mid-latitude baroclinic cyclone.

Type 1 (clusters 1, 2, and 5) has been frequently mentioned as a typical synoptic SLP pattern responsible for the springtime DW events in the YD in Korea in many previous studies. We found that this pattern is accompanied by warm advection at 850 hPa (about $z = 1.5$ km), so an inversion layer is able to be formed near the top of the TM ($z = 1{-}1.5$ km in Fig. 1) especially when there is surface cooling at night in this pattern. On the other hand, cold advection at 850 hPa and the lower troposphere in Type 2 (clusters 3, 4, and 8) can also provide favorable conditions for an inversion layer at the top of Planetary Boundary Layer (PBL) (typically around $z = 1{-}1.5$ km) when there is surface heating in the daytime. These atmospheric structures with inversion layers at the top of the mountains provide favorable conditions for DWs (Durran 1990;

Wang and Lin 2000; Vosper 2004; Lee and In 2009; Decker and Robinson 2011), which can promote the optimal superposition of mountain waves that are partially reflected at levels of sudden change in atmospheric stability (Klemp and Lilly 1975) and hydraulic jump on the lee slope by enhancing wind speed (Long 1953). More details are provided in Section 6.

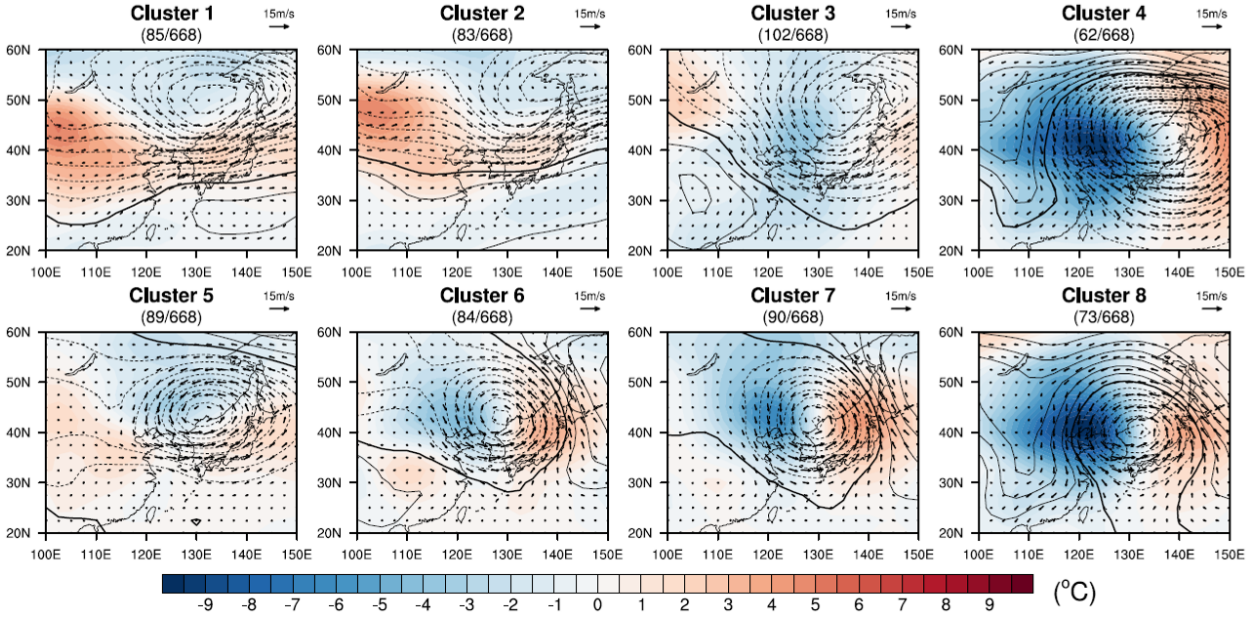

Figure 6. The 850 hPa geopotential height (solid and dashed lines for positive and negative values, respectively, in the interval of 10 m), temperature (shading), and horizontal wind (arrow) anomalies averaged within each cluster.

5 Adiabatic warming Effect

DWs with adiabatic warming on a lee slope cause extremely dry and warm conditions, thus making them highly related to wildfires, especially in the springtime in the YD in combination with drought conditions in this area. In order to understand which synoptic pattern can provide more vulnerable conditions for wildfires via DW events, temporal changes in surface temperature anomalies were investigated. The surface temperatures measured at GN and DGL shown in Fig. 1 were considered because GN is a city located on the lee side of the mountains and DGL is located on a mountain top of the TM at an altitude of approximately 750 m. SC was not considered here because there were no long-term ASOS data measured at the station located at the top of the TM to the west of SC, so DW events that occurred when strong winds were only observed in SC were excluded in this analysis. Here, temperature anomalies were calculated by subtracting monthly and hourly mean temperatures from measured values to remove both seasonal and diurnal variations as well as to analyze the impact of DWs. For example, we subtracted the mean surface temperatures of April 06 UTC measured at each station for 41 years from all temperature data measured in April 06 UTC. This method was used because there were no continuously observed surface temperature data over this period with a high enough temporal resolution to obtain temperature perturbation by Reynolds averaging over a few tens of minutes, and we wanted to investigate not only the temperature differences between GN and DGL but also temperature change over time at each station.

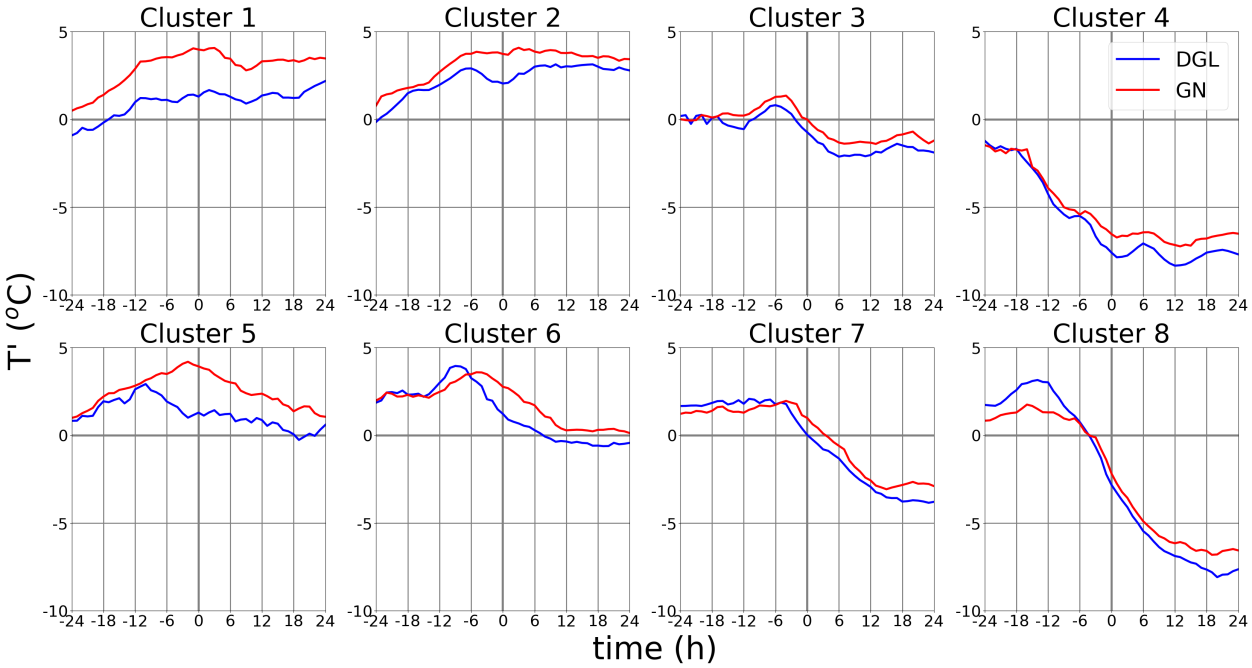

Figure 7. Temporal changes in surface temperature anomalies at Gangneung (GN; in the downstream of Taebaek Mountains; red) and Daegwallyeong (DGL; on Taebaek Mountains; blue). Data for ±24 hours around the observed maximum instantaneous wind speeds are shown.

Figure 7 shows temporal changes in surface temperature anomalies at GN and DGL for ±24 hours around the DW event. Note that the maximum daily wind speed was measured at GN in the middle of each DW event, and temperature anomalies were averaged for the events when the daily maximum instantaneous wind speed at GN exceeded 20 m s^{-1} in each cluster. Temperature anomalies at GN at the time of the maximum wind speeds were found to be the highest in cluster 1 and the lowest in cluster 4, and these values decreased from the left to the right in the node array. This shows that surface temperature at GN is larger than usual in Type 1 (clusters 1, 2, and 5), and smaller than usual in Type 2 (clusters 3, 4, and 8). In Type 3 (clusters 6 and 7), surface temperature was found to be similar to usual values. Additionally, surface temperature anomalies increased at both sites as the maximum wind time approached in Type 1, but they decreased in Type 2. In Type 3, temperature anomalies increased before the maximum wind time and then increased after. Considering the 850 hPa synoptic field analysis in Section 4.3, it can be estimated that synoptic-scale temperature advection in each pattern contributed to this result. In Type 1, the increase in surface temperature was found to be larger than usual due to synoptic warm advection. In Type 2, temperature was found to decrease more than usual due to synoptic cold advection. In Type 3, temperature was found to increase and then decrease due to temperature advection around the baroclinic cyclone. Additionally, the increase or decrease in temperature anomalies was larger when the magnitude of synoptic temperature advection was greater.

In general, surface temperature anomalies were found to be larger in GN than in DGL as the maximum wind time approachd in all clusters. However, the difference was found to be much larger in Type 1 near the maximum wind time than any other types. This means that

449 temperature is likely to increase when a flow goes from DGL (mountain top) to GN (lee side).
450 This increase was found to be the largest in Type 1, implying that temperature increases due to
451 the adiabatic warming of descending air flow along the DW on the lee slope of the TM (i.e., the
452 Föhn effect). In summary, the temporal change in surface temperature anomalies at GN and DGL
453 reflect the synoptic temperature advection at the 850 hPa level, and the larger temperature
454 anomalies in GN imply that the warming effect due to the downslope wind on the lee side and it
455 is the strongest in Type 1. This type is a typical pattern of springtime DWs in the YD that has
456 frequently been mentioned in many previous studies. Additionally, the results of this section
457 reveal that the warm and dry characteristics of strong winds in this type rapidly promote the
458 spread of severe wildfires when they occur in this region (Kim and Chung 2006; Jang and Chun
459 2010).

460 **6 Mesoscale Mechanisms**

461 Under the classified synoptic-scale conditions described in previous sections, we
462 examined how DW events can be explained by the three representative mesoscale mechanisms:
463 hydraulic jump theory, partial reflection of mountain waves, and critical level reflection with
464 wave breaking. We calculated zonal wind speed perpendicular to the mountain range and
465 atmospheric stability under the corresponding clusters for ±3 hours around DW events. Then, we
466 found events that satisfied the conditions of each mechanism and compare their ratio within each
467 cluster.

468 6.1 Hydraulic Jump Theory

469 Hydraulic jump occurs when a subcritical flow in the upstream of a barrier changes to a
470 supercritical one on the crest or lee slope of a barrier (Long 1954). The critical state is
471 determined by the Froude number (Fr), which is calculated by the velocity, stability, and depth
472 of the upstream flow. If Fr is above (or below) a critical value, the flow is supercritical (or
473 subcritical). Different flow regimes with or without hydraulic jumps in the lee side can be
474 identified by the following two methods.

475 6.1.1 Froude Number in a Shallow Water

476 By considering one-dimensional flow with a free surface or a rigid upper boundary over
477 an isolated barrier, the motion of a fluid is governed by shallow water equations (Houghton and
478 Kasahara 1968). In this case, the occurrence of hydraulic jumps is determined by Fr and the
479 nondimensional height M, defined as follows:

480 $$Fr = \frac{U}{\sqrt{g\frac{\Delta\theta}{\theta_0}h}}, \quad (4)$$

481 $$M = \frac{H}{h}, \quad (5)$$

482 where U is the velocity of fluid, g is gravitational acceleration, θ_0 is potential
483 temperature of fluid, $\Delta\theta$ is the difference in potential temperature between the two layers, h is
484 the depth of fluid and H is the mountain height. Here, H = 1114.543 m, which was calculated by
485 averaging the zonal maximum height of the TM (Fig. 1). If Fr in upstream is moderately
486 subcritical and the flow is not too deep compared to the height of the barrier, the flow becomes
487 supercritical in the downstream (Long 1954). This supercritical state is achieved if the governing

equations of the motion reveal discontinuous jumps on the upper surface, because they cannot obtain physically meaningful solutions when Fr and M satisfy the following condition:

$$M > M_*, \quad (6)$$

where $M_* = \frac{Fr^2}{2} - \frac{3}{2}Fr^{2/3} + 1$ is a critical value of M (Houghton and Kasahara 1968).

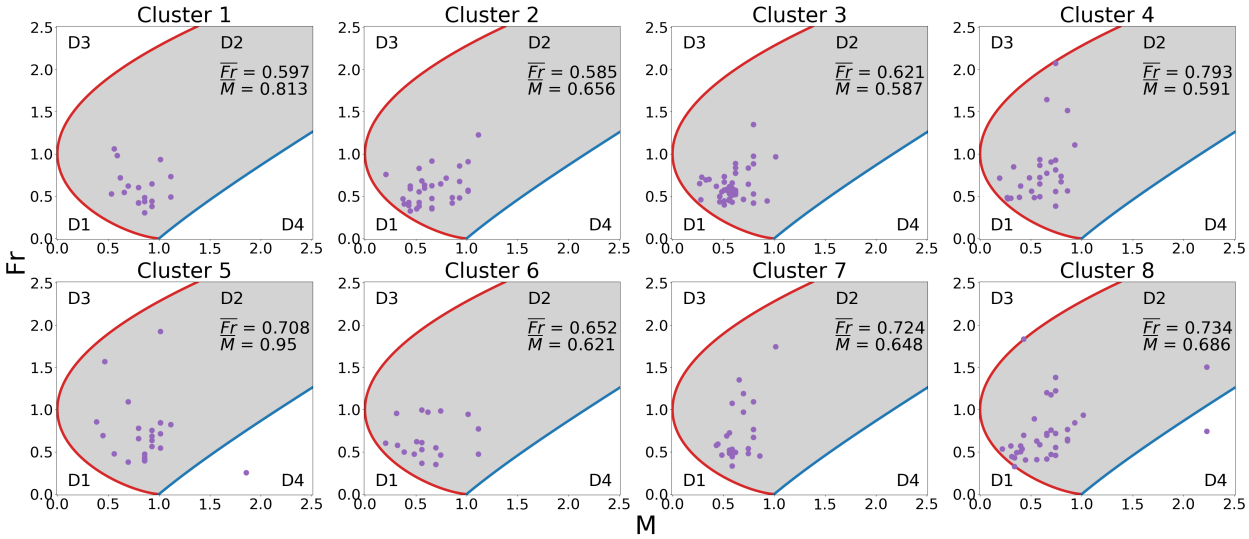

Figure 8. Fr–M diagrams with points of downslope windstorm (DW) events with inversion layers in upstream in each cluster. Red and blue lines indicate a critical value of M $\left(M_* = \frac{Fr^2}{2} - \frac{3}{2}Fr^{2/3} + 1\right)$ and Fr of total blocking $\left(Fr = \frac{M-1}{M}\sqrt{\frac{M(M+1)}{2}}\right)$, respecitvely. The points in domain 2 (D2 of the shaded areas) indicate hydraulic jumps.

Figure 8 shows Fr–M diagrams with a red curve indicating M_* and a blue straight line of total blocking indicating $Fr = \frac{M-1}{M}\sqrt{\frac{M(M+1)}{2}}$ (Houghton and Kasahara 1968) in each cluster. In domains 1 and 3 (D1 and D3, respectively, in Fig. 8), real solutions can exist without discontinuous jumps because $M < M_*$ (i.e., no hydraulic jump). In domain 4 (D4 in Fig. 8), the flow is completely blocked by the mountain. In domain 2 (D2 of the shaded areas in Fig. 8), no solution can exist without a discontinuous jump because $M > M_*$, meaning that the flow must have discontinuous jumps to satisfy the governing equations. Therefore, the cases in D2 have a hydraulic jump on the lee side with a transition from subcritical to supercritical flow.

Since the flow should have a free surface or a rigid upper boundary to be expressed as shallow water equations, Fr can only be calculated when there is an inversion layer. Additionally, hydraulic jumps cannot occur if the depth of the fluid is much larger than the mountain (Long 1954), so the top height of the inversion layer was set to be below z = 6000 m (which is approximately five times the height of the mountain) in this study. When we calculated the frequency of the existence of the hydraulic jump and the inversion layer, as shown in Fig. 9, most cases with inversion layers were found to be in the regime of hydraulic jumps (D2 in Fig. 8), implying that hydraulic jumps mostly occur when there are inversion layers below z = 6000

514 m. In addition, Fig. 9 shows that the frequency of hydraulic jump cases was found to be
515 significantly (more than two times) higher in Type 2 (clusters 3, 4, and 8) than other types.
516 Therefore, DW events in Type 2 are more likely to be explained by the hydraulic jump theory,
517 with the more frequent existence of inversion layers acting as a rigid upper bound of flow.

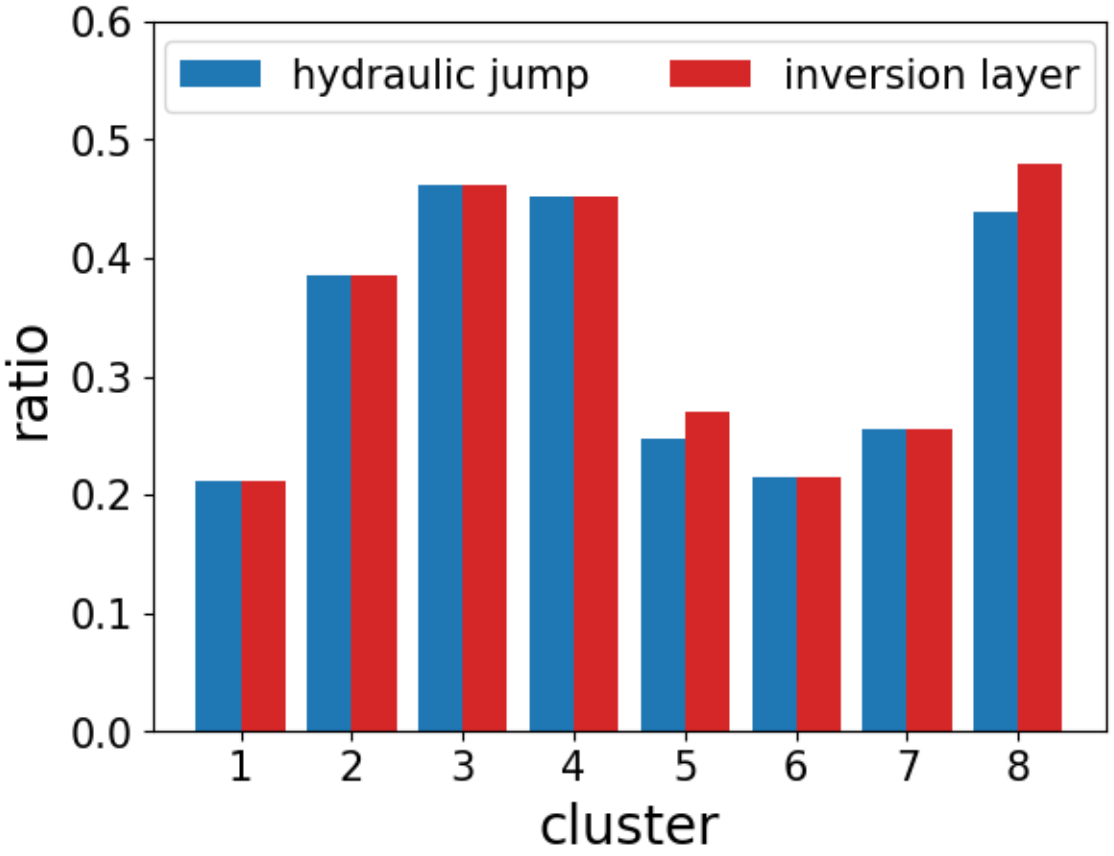

518

519 **Figure 9**. The ratio of downslope windstorm (DW) events explained by hydraulic jump theory
520 (blue) and with inversion layers in upstream (red) in each cluster.

521

522 The results in Figs. 8 and 9 reveal that DW events with hydraulic jumps in wintertime
523 patterns are more likely to occur under background conditions with frequent inversion layers in
524 the lower troposphere. In those patterns, the lowest layer of the atmosphere was found to be less
525 stable, as shown by their nearly neutral potential temperature profiles and lower N^2 values below
526 z = 1500 m (blue lines in Fig. 10b, c), which was possibly due to the mixing in the PBL when
527 cold advection was dominant just above relatively warm surface with surface heating in the
528 daytime. The mid-troposphere was more stable and zonal wind is stronger in wintertime patterns
529 than other patterns, shown as more rapidly increasing wind and potential temperature with height
530 and higher N^2 values above z = 1500 m (blue lines in Fig. 10a–c). Large changes in wind and
531 static stability between two layers (lower- and mid-troposphere) were found to contribute to the
532 formation of inversion layers as their interfaces. Nevertheless, this result does not mean that
533 inversion layers do not exist in the other patterns because the cause of the formation of inversion
534 layers and their effects on strengthening DWs are different in each pattern.

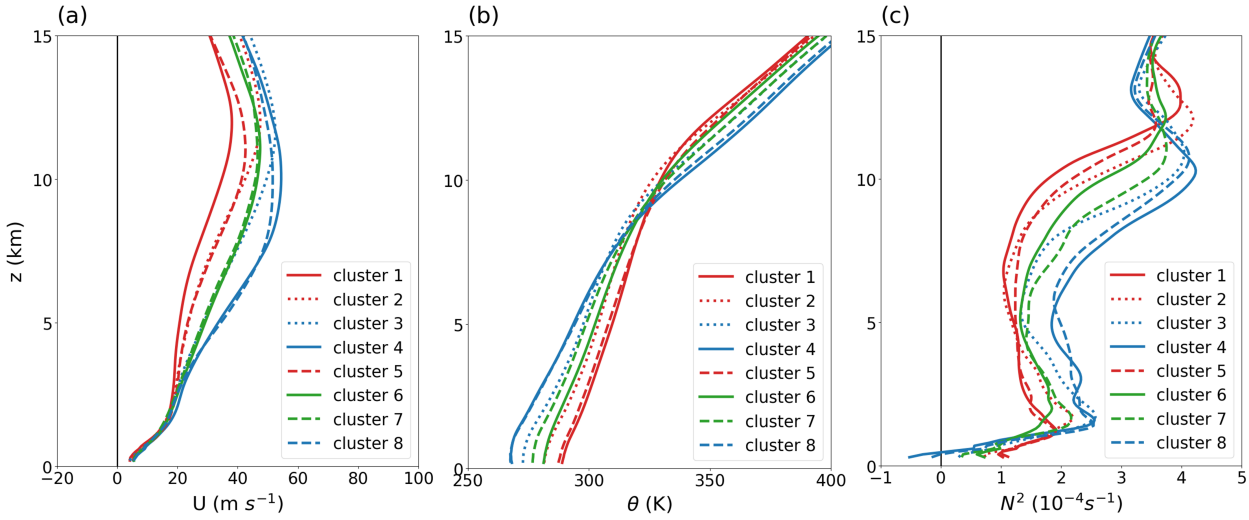

Figure 10. Vertical profiles of (a) zonal wind speed, (b) potential temperature, and (c) Brunt–Väisälä frequency averaged in upstream in each cluster. Red, blue, and green lines indicate Type 1 (clusters 1, 2, and 5), 2 (clusters 3, 4, and 8), and 3 (clusters 6 and 7), respectively.

6.1.2 Froude Number in a Stratified Flow

The second method to determine the flow regimes related to hydraulic jumps is to calculate Fr in the upstream by assuming that the flow has uniform wind speed and static stability with height, as follows:

$$Fr = \frac{U}{NH}, \quad (7)$$

where U and N are, respectively, the wind speed and Brunt–Väisälä frequency, and where H is the mountain height. Hydraulic jumps in continuously stratified fluid do not require a rigid lid or discontinuity in flow (Durran 1986; Lin and Wang 1996). Durran (1986) stated that the transition from subcritical to supercritical flow produces high velocities along the lee slope by converting potential energy to kinetic energy if there is sufficient acceleration toward a mountain. Lin and Wang (1996) identified four different regimes for two-dimensional stratified flow over an isolated mountain range as follows: 1) there is neither downstream wave breaking nor upstream blocking, so the waves are linear or weakly nonlinear in the absence of lee jumps ($Fr \geq 1.12$); 2) wave breaking occurs aloft without upstream blocking, and the lee jump propagates downstream to cause severe DWs ($0.9 \leq Fr \leq 1.12$); 3) wave breaking occurs earlier than upstream blocking, and the lee jump becomes quasi-stationary, thus causing severe DWs ($0.6 \leq Fr \leq 0.9$); and 4) upstream blocking occurs earlier than wave breaking and the lee jump is weak ($0.3 \leq Fr \leq 0.6$). These regimes are consistent with the work of Long (1954), who found that moderate upstream Fr values in the second and third regimes cause hydraulic jumps.

Here, we calculated Fr by averaging U and N from the surface to 1500 m because in a real flow they are not uniform with height. We tried using various layer top heights averaging U and N to test its sensitivity to Fr, and we found systematic increases in Fr and height, possibly due to the increasing U with height in the mid-latitudes. Finally, we chose 1500 m, because it is

slightly above the top of TM, so the airflow below this level is mostly affected by the mountains. This value was also used in previous studies on DW events in the YD (Kim and Chung 2006; Jang and Chun 2008). Note that here, Fr was calculated for all events including those without inversion layers, unlike the method used in Section 6.1.1. Then, we investigated the ratio of the events in each flow regime following Lin and Wang (1996) explained above: 1) the jump is too weak to generate the severe DWs in the downstream ($0.3 \leq Fr \leq 0.6$); 2) significant hydraulic jumps cause severe DWs ($0.6 \leq Fr \leq 1.12$); and 3) flow is so linear that it does not produce hydraulic jumps ($Fr \geq 1.12$). Here, the second ($0.9 \leq Fr \leq 1.12$) and third ($0.6 \leq Fr \leq 0.9$) flow regimes of Lin and Wang (1996) were combined into one because both regimes commonly have hydraulic jumps with severe DWs in the lee side.

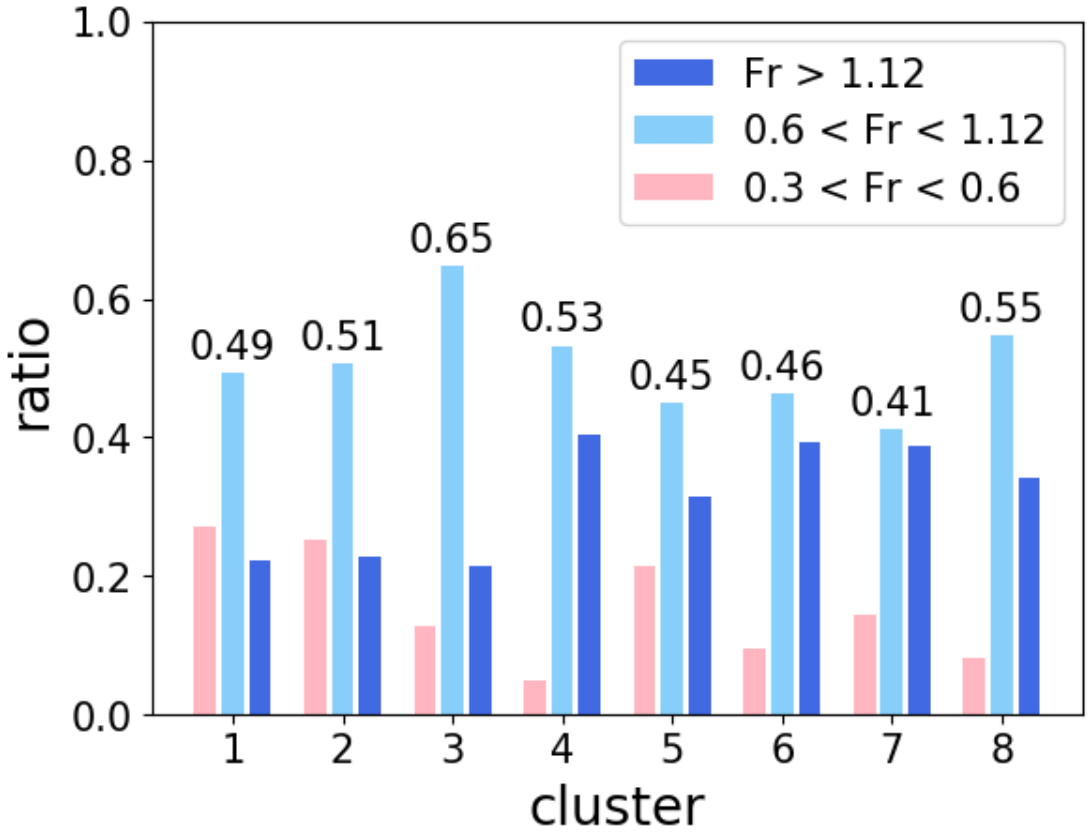

Figure 11. The ratio of downslope windstorm (DW) events in highly nonlinear flow regime with weak jumps ($Fr \geq 1.12$; pink bars), moderate flow regime with significant lee jumps and severe winds ($0.6 \leq Fr \leq 1.12$; skyblue bars with numbers), and linear flow regime without lee jumps ($0.3 \leq Fr \leq 0.6$; blue bars).

Figure 11 shows the ratio of the cases for three different flow regimes in each cluster. The ratios of the strong hydraulic jump regime ($0.6 \leq Fr \leq 1.12$; skyblue bars in Fig. 11) are 0.4–0.7 in the clusters, which are slightly higher than 0.39, the ratio of hydraulic jumps to springtime DWs in Jang and Chun (2008). In particular, clusters 3, 4, and 8 in Type 2 showed the first (69%), second (62%), and fourth highest (50%) ratio of lee jumps, respectively. This is consistent with the results shown in Figs. 9 and 10, where it can be seen that the Type 2 has more

586 frequent strong hydraulic jump regimes with moderate Fr values. The frequencies in the linear
587 flow regime ($Fr \geq 1.12$; blue bars in Fig. 11) were also relatively larger in Types 2 and 3
588 compared to Type 1, meaning that the inflow (and thus downstream flow) was already
589 supercritical. The frequencies in the weak jump regime ($0.3 \leq Fr \leq 0.6$; pink bars in Fig. 11) in
590 Type 1 (clusters 1, 2, and 5) were found to be significantly larger than those in other types.
591 Under the Type 1 pattern of the south high- and north low-pressure systems around Korea in the
592 springtime, Fr is not large enough to produce significant lee jumps and severe DWs, implying
593 that there must be other mechanisms related to the high frequency of DWs in the springtime;
594 these are examined in the following sections.

595 In summary, the significant hydraulic jumps responsible for severe winds on the lee slope
596 were found to be more frequent in wintertime patterns than in the other patterns due to the more
597 frequent occurrence of moderate Fr values. Type 1 was found to have small numbers of
598 hydraulic jump cases due to large number of cases in a weak jump regime, and Type 3 was
599 because it was found to have both many large and small Fr cases. These results can be explained
600 by mean vertical profiles of zonal wind speed, potential temperature and Brunt–Väisälä
601 frequency in Fig. 10 and by box plots of Fr, U, and N in Fig. 12. Zonal wind was found to be
602 stronger in all levels in the wintertime patterns than the others (Fig. 10a), meaning that U is
603 higher in this pattern (Fig. 12b). Lower troposphere below 1500 m was found to be less stable in
604 the wintertime patterns (Fig. 10b, c), so N is smaller in this pattern than others (Fig. 12c).
605 Therefore, in wintertime patterns, the higher Fr (Fig. 12a), which is resulted in slightly higher U
606 (Fig. 12b) and much lower N (Fig. 12c), causes more events to be included in the strong
607 hydraulic jump regimes.

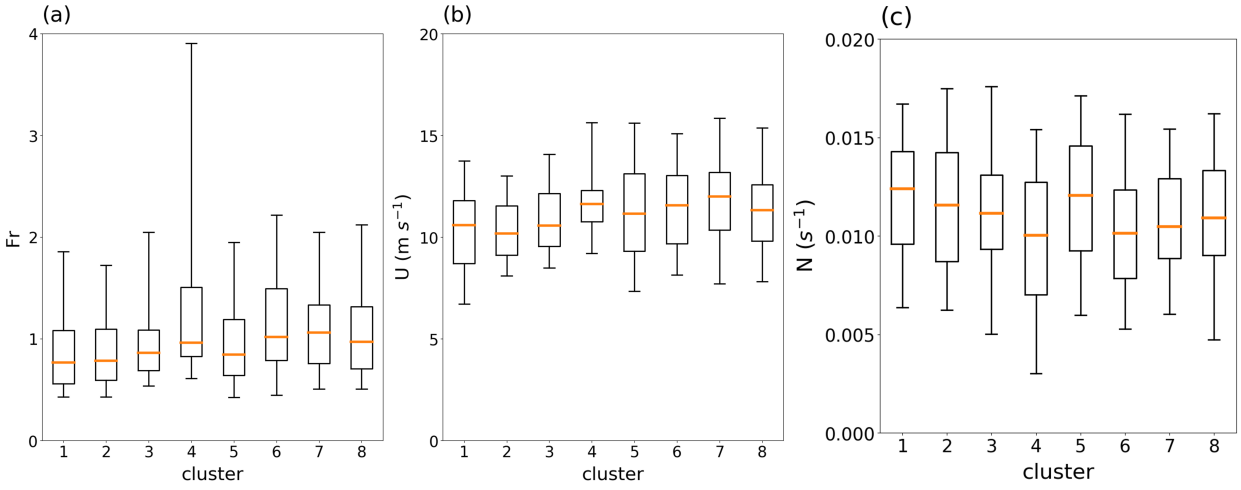

608

609 **Figure 12**. Box plots of (a) Fr, (b) U, and (c) N in each cluster. Orange solid lines indicate the
610 medians. Boxes include from the 1st to 3rd quartiles, and whiskers indicate the 5th and 95th
611 percentiles.

612 6.2 Partial Reflection of Mountain Waves

613 Klemp and Lilly (1975) suggested that upward-propagating mountain waves can be
614 partially reflected if the Scorer parameter rapidly changes due to variations in wind and thermal
615 stability. Then, the optimal superposition of upward- and downward-propagating waves can
616 transport the reflected energy and amplify surface wind speed downstream of mountains. This

generation mechanism of DW is called the partial reflection of mountain waves. Though this is drawn by a linear multi-layer model with idealized vertical profiles where wind and stability are constant in each layer, we calculated the Scorer parameter l of vertically varying wind and stability to identify the vertical structure of mountain waves in real cases, as illustrated below:

$$l^2 = \frac{N^2}{U^2} - \frac{1}{U}\frac{d^2U}{dz^2}, \quad (8)$$

where U and N are zonal wind speed and Brunt–Väisälä frequency at each vertical level, respectively (Scorer 1949). The square of the Scorer parameter is the sum of the square of horizontal and vertical wavenumber (k and m, respectively), and we used this value to obtain the square of the vertical wavenumber ($m^2 = l^2 - k^2$) at each level. In this calculation, we assumed that the horizontal wavelengths could vary from 5 to 50 km based on previous studies on DW (Jang and Chun 2008; 2010) and mountain wave-induced turbulence (Kim and Chun 2010) in this region, which showed that the dominant horizontal wavelengths of the mountain waves were approximately 10–25 km. Finally, following the work of Jang and Chun (2008; 2010), whether a level of trapped mountain waves with negative vertical wavenumber ($m^2 < 0$) exists in each case was examined. Here, the partial reflection mechanism was investigated by examining the existence of the reflection of vertically propagating mountain waves (i.e., $m^2 < 0$). Additional conditions for the optimal superposition of waves generating severe DWs were not tested because 1) the real vertical structures of the atmosphere are too different from idealized ones for comparison to the multi-layer model generating partial reflection and resonance of waves, and 2) vertical wavelengths varying with heights become infinite near the levels of zero vertical wavenumbers, which makes it hard to identify the optimal conditions for the resonance of waves. Note that reflection levels were found above z = 2000 m because the variation in the wind curvature term in the Scorer parameter was found to be too large due to the wind shear in the lower troposphere; consequently, no waves can grow above this layer.

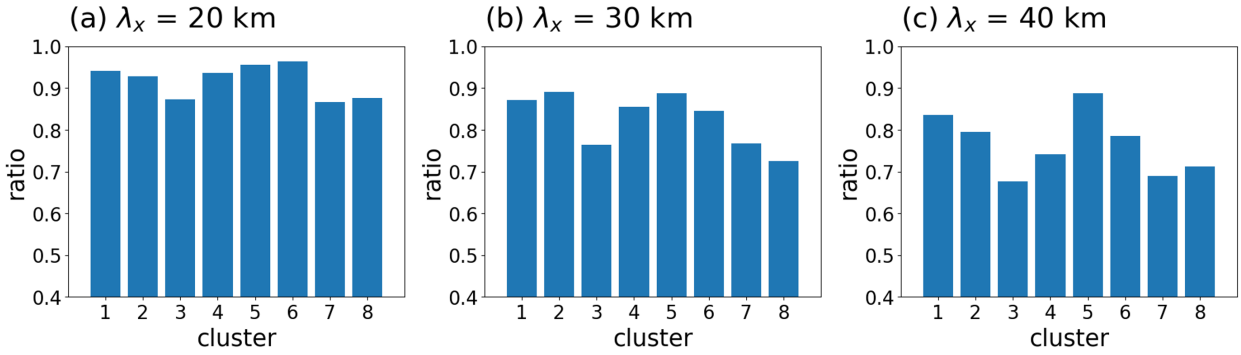

Figure 13. The ratio of downslope windstorm (DW) events generated by partial reflection of mountain waves with horizontal wavelengths of (a) 20 km, (b) 30 km, and (c) 40 km in each cluster.

Figure 13 shows the ratio of cases with reflected mountain waves in each cluster when horizontal wavelengths were set to 20, 30, and 40 km (Fig. 13a, b, c, respectively). DW events in springtime patterns are more often generated by the reflection of mountain waves than those in wintertime patterns. This is because clusters in Type 1 (frequent in the spring) have larger ratios than those in Type 2 (frequent in the winter); additionally, cluster 6 (relatively frequent in the spring) was found to have a larger ratio than cluster 7 (relatively frequent the in winter) in Type 3. In addition, the difference in the ratios between springtime and wintertime patterns was found

to become larger as the horizontal wavelengths became longer. This implies that in springtime patterns, there are more cases related to the reflection of short-to-long mountain waves and, consequently, more energy transported to the surface. Meanwhile large-scale mountain waves in wintertime patterns can propagate to the upper atmosphere and remain unfiltered in the upper-level (Kim and Chun 2010) in many cases due to the large vertical wavenumber of the large horizontal wavelength without their energy being transported to the surface.

In Fig. 10a, mean wind speed can be seen to be relatively weaker in all levels in springtime patterns than wintertime patterns, but stability in the mid-troposphere can be seen to be much lower in springtime patterns than wintertime patterns. When considering the first term on the right hand side of Eq. 8, significant reduction of stability, especially in the mid-troposphere in springtime patterns, is likely related to conditions for the partial reflection of waves and responsible for trapped lee waves associated with DWs (Kim and Chun 2010). Nevertheless, the overall ratios of reflected waves were found to be 0.8–0.9, suggesting that the partial reflection of mountain waves occur in most DW cases, which is consistent with the work of Jang and Chun (2008) showing that 84% of springtime DWs were related to the partial reflection of mountain waves. This is probably because levels of sudden change in static stability or wind curvature have existed in most cases. Static stability in the atmosphere rapidly changes near an inversion layer, and wind curvature increases strongly below a jet stream. These atmospheric structures are likely to be common in many DW cases, so the reflection of mountain waves and downward energy transport occur in most DW cases.

6.3 Critical Level Reflection with Wave Breaking

Clark and Peltier (1984) suggested that vertically propagating mountain waves are reflected in the presence of a background or wave-induced critical level with a reversal of wind direction and a Richardson number (Ri) smaller than 0.25 near the critical level. If the ratio of the critical level height to the vertical wavelength is $n + \frac{3}{4}$ $(n = 0, 1, 2, \cdots)$, the constructive superposition of incident and reflected waves can cause resonantly amplified wind speed near the surface by increasing surface wave drags. We determined DW events with wave breaking at critical levels via the following procedures. First, the existence of reversed flow was examined. The cases with easterly flow at the points above the lee sides of mountains and westerly flow below for ±3 hours around the DW events were identified as critical levels for stationary mountain waves. Finding the local regions of flow reversal with height indicated the wave breaking of vertically propagating stationary mountain waves. Second, the Ri near the critical level (i.e., local region of wind reversal) was considered. Though the critical level reflection was found to occur when $Ri < 0.25$ in a stably stratified flow (Howard 1961; Miles 1961), we identified the cases with $Ri < 1$near the reversed flow as the critical level reflection, because in the three-dimensional flow of real atmosphere (i.e., nonlinear flow), the stable condition of flow is often violated even when $Ri < 1$ (Abarbanel et al. 1984; 1986; Miles 1986).

Figure 14a, b shows the ratio of DW events with a critical level or reflection above z = 4000 and 8000 m in each cluster, respectively. The overall ratio can be seen to have been very small, approximately 10%, because the flow in the upper-troposphere was usually strong westerly in the mid-latitudes, and the ERA5 data do not have a good enough vertical and horizontal resolution to fully resolve vertically propagating mesoscale mountain waves and their subsequent self-induced critical levels by breaking large amplitude waves. This result is similar

to that of Jang and Chun (2008), who showed that only about 5% of springtime DW events in this region had a critical level by examining upstream sounding data. Comparing the ratios between clusters revealed that critical levels are produced and critical level reflections occur ($Ri < 1$) most frequently in cluster 1 (Type 1), which is a south high and north low pattern in the spring. Though some cases in clusters 3, 6, 7, and 8 were found to have critical levels, there were no critical levels in the upper atmosphere in most cases. Most critical levels in cluster 1 were found to exist above 8000 m. Additionally, the ratio of critical level reflection ($Ri < 1$) was found to be the highest in cluster 1. In summary, both the existence of critical levels in the upper layer and the occurrence of critical level reflection due to instability were found to be the most frequent in the south high and north low pattern in cluster 1, so DWs generated by critical level reflection and wave breaking are most likely to be included in this pattern. This is partly because upper-level winds that are weaker in springtime patterns (red lines in Fig. 10a) than in wintertime patterns (blue lines in Fig. 10a) create better conditions for the critical level of high amplitude vertically propagating mountain waves, and their subsequent breakdowns can provide more chances to have small but positive Ri values inducive to shear instability and/or negative Ri values for convective instability due to the overturning of isentropes, which results in critical level reflection and strong DW events near the surface in the downstream. Thus, most DW cases with a critical level with small Ri and critical level reflection are in cluster 1, the south high and north low pattern.

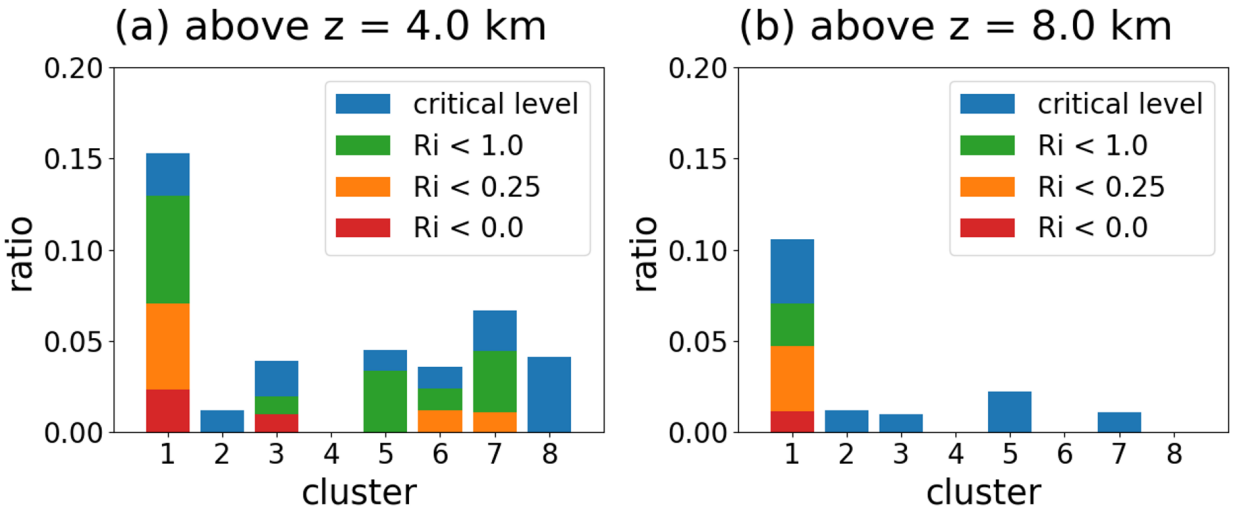

Figure 14. The ratio of downslope windstorm (DW) events generated by wave breaking at critical levels above z = 4 km (a) and 8 km (b). Green, orange, and red bars indicate that Ri near the critical level are below 1, 0.25, and 0, respectively.

7 Conclusions

Downslope windstorms (DWs) are severe winds generated when a flow across a mountain is accelerated on the lee side. They are typically generated by hydraulic jumps, partial reflections of mountain waves, and critical level reflections with wave breaking. DWs often occur in the springtime and the wintertime in Yeongdong region (YD), located on the lee side of the Taebaek Mountains (TM) in Korea, and they are frequently responsible for disasters such as wildfires and low level turbulence. At the PyeongChang 2018 Olympic and Paralympic winter

games, there was a DW event that caused structural damage to and the cancellations of some outdoor games such as the ski jump and biathlon on 14–15 Feb 2018. The YD was the main area for the International Collaborative Experiments for the PyeongChang 2018 Olympic and Paralympic winter games (ICE-POP 2018). Previous studies have shown that when DWs associated with wildfires occur in this region, south high and north low synoptic SLP patterns have frequently been observed and accompanied by warm advection and an inversion layer near the top of the mountains (Kim and Chung 2006; Jang and Chun 2010).

Here, we used an unsupervised neural network algorithm, a self-organizing map (SOM), to classify synoptic SLP patterns responsible for the DW events found in 41 years of records. We found that the optimal number of clusters is eight, which is where the ECV begins to be saturated and the TE has a local minimum, implying that individual clusters are well separated. Those eight clusters can be categorized into three representative types: 1) the south high and north low pattern, 2) the west high and east low pattern, and 3) the strong low pressure system passing in the northern part of Korea. The monthly distribution in each cluster shows that the occurrence of Type 1 is dominant in the springtime, the occurrence of Type 2 is dominant in the wintertime, and Type 3 occurs in both spring and winter. At the 850 hPa level, near the top of the TM, prevailing southwesterly flow with warm advection can be found in Type 1, while prevailing northwesterly flow with cold advection can be found in Type 2. Cold and warm advection can be found in the back and front of the center of low respectively in Type 3, indicating that the low-pressure system is baroclinic and well-developed.

Surface temperature anomalies both on the lee side of the mountain and on the mountain were found to increase in Type 1 but decrease in the other types when the maximum wind speed was measured due to synoptic temperature advection over the Korean Peninsula. Additionally, the surface temperature anomalies were found to be larger on the lee side of the mountain than on the mountain in all clusters, but the difference was found to be the largest in Type 1. This suggests that the adiabatic warming via descending air flow in the downstream of the mountain (i.e., the Föhn effect) is the highest in Type 1, implying that warm and dry air with strong winds can more frequently contribute to the rapid spread of severe wildfires in this area in the springtime (dry season).

We investigated how the mesoscale mechanisms responsible for DWs are different under the classified weather patterns. Here, the representative mesoscale generation mechanisms for the DWs are hydraulic jumps, partial reflections of mountain waves, and wave breaking at critical levels. More events explained by hydraulic jump theory were found to be in Type 2 than other types because upstream flows with moderately subcritical Froude number (Fr) and inversion layers were more frequently observed. Meanwhile, we found more events to be generated by partially reflected mountain waves in springtime patterns (Type 1 and cluster 6 in Type 3) than in wintertime patterns (Type 2 and cluster 7 in Type 3) for a wide range of horizontal wavelengths used to calculate the vertical wavenumber, although the partial reflection of mountain waves was found to be related to most DW events in general. In addition, most DW events with critical level reflection and wave breaking in the upper troposphere were found to occur in cluster 1 in Type 1.

This study reveals that springtime DW events occur under the south high and north low SLP pattern (Type 1) with relatively more chances of generation mechanisms related to mountain waves such as partial reflection and critical level reflection. This type causes a stronger Föhn effect (i.e., adiabatic warming), resulting in drier and warmer air on the lee side, which is

associated with strong wildfires in the YD in the springtime. On the other hand, wintertime DW events were found to occur under the west high and east low SLP pattern (Type 2), which includes cold advection in the lower troposphere that enhances PBL mixing and an inversion layer at the top of the PBL. This provides favorable conditions for hydraulic jumps. Both these two patterns and the strong low pattern in the East Sea of Korea (Type 3) can generate DWs in both spring and winter.

For future work, DW events under the different synoptic SLP patterns classified in this study will be investigated in more detail via high resolution numerical model simulation because there are still several local factors such as the channeling effect and drainage flow that may explain extreme winds embedded in the DW events in local areas. Since there would be a limitation in analyzing detailed atmospheric flows solely using the large-scale weather patterns in this study, detailed vertical structures of DWs and propagating mountain waves in concert with local effects by resolved and unresolved topography as well as numerical mesoscale model simulation with a high resolution are required to address these problems, so that we may eventually provide more fine-scale structures of turbulence during DW events in the YD under different regimes. Nevertheless, this study suggests that DWs in the YD in Korea can be classified via objective synoptic SLP patterns using a machine learning algorithm (SOM). Additionally, the types of DWs show inherent differences in the characteristics of background wind and stability, resulting in different contributions to generation mechanisms. This objective classification of DW events in the YD will eventually be very useful in providing baseline information for better predictions and future projections of DW events in this area.

Acknowledgments

This research was supported by the Basic Science Research Program through the National Research Foundation of Korea (NRF), funded by the Ministry of Education. (NRF-2019R1I1A2A01060035).

Data Availability Statement

The Self-Organizing Map (SOM) toolbox can be download at http://www.cis.hut.fi/projects/somtoolbox/. The automated surface observing system (ASOS) data in South Korea are available at the following website (in Korean): https://data.kma.go.kr/data/grnd/selectAsosRltmList.do?pgmNo=36. The National Centers for Environmental Prediction–Department of Energy (NCEP–DOE) Reanalysis 2 data can be obtained from https://psl.noaa.gov/data/gridded/data.ncep.reanalysis2.html. Fifth-generation ECMWF reanalysis (ERA5) hourly data on pressure levels are available from https://cds.climate.copernicus.eu/cdsapp#!/dataset/reanalysis-era5-pressure-levels?tab=overview.

References

Abarbanel, H. D., Holm, D. D., Marsden, J. E., & Ratiu, T. (1984). Richardson number criterion for the nonlinear stability of three-dimensional stratified flow. Physical Review Letters, 52(26), 2352. https://doi.org/10.1103/PhysRevLett.52.2352

Abarbanel, H. D., Holm, D. D., Marsden, J. E., & Ratiu, T. S. (1986). Nonlinear stability analysis of stratified fluid equilibria. Philosophical Transactions of the Royal Society of London. Series A, Mathematical and Physical Sciences, 318(1543), 349-409. https://doi.org/10.1098/rsta.1986.0078

Cho, Y.-J., Kwon, T.-Y., & Choi, B.-C. (2015). Characteristics of Meteorological Variables in the Leeward Side associated with the Downslope Windstorm over the Yeongdong Region. Journal of the Korean Earth Science Society, 36(4), 315-329. https://doi.org/10.5467/JKESS.2015.36.4.315 (In Korean with English Abstract)

Cho, Y.-J., Lee, H.-C., Lim, B., & Kim, S.-B. (2019). Classification of Weather Patterns in the East Asia Region using the K-means Clustering Analysis. Atmosphere, 29(4), 451-461. https://doi.org/10.14191/Atmos.2019.29.4.451

Clark, T. L., & Peltier, W. R. (1984). Critical level reflection and the resonant growth of nonlinear mountain waves. Journal of Atmospheric Sciences, 41(21), 3122-3134. https://doi.org/10.1175/1520-0469(1984)041<3122:CLRATR>2.0.CO;2

Decker, S. G., & Robinson, D. A. (2011). Unexpected high winds in northern New Jersey: A downslope windstorm in modest topography. Weather and forecasting, 26(6), 902-921. https://doi.org/10.1175/WAF-D-10-05052.1

Durran, D. R. (1986). Another look at downslope windstorms. Part I: The development of analogs to supercritical flow in an infinitely deep, continuously stratified fluid. Journal of Atmospheric Sciences, 43(21), 2527-2543. https://doi.org/10.1175/1520-0469(1986)043<2527:ALADWP>2.0.CO;2

Durran, D. R. (1990). Mountain waves and downslope winds. In Atmospheric processes over complex terrain (pp. 59-81). American Meteorological Society, Boston, MA. https://doi.org/10.1007/978-1-935704-25-6_4

Glisan, J. M., Gutowski Jr, W. J., Cassano, J. J., Cassano, E. N., & Seefeldt, M. W. (2016). Analysis of WRF extreme daily precipitation over Alaska using self-organizing maps. Journal of Geophysical Research: Atmospheres, 121(13), 7746-7761. https://doi.org/10.1002/2016JD024822

Hoinka, K. P. (1985). Observation of the airflow over the Alps during a foehn event. Quarterly Journal of the Royal Meteorological Society, 111(467), 199-224. https://doi.org/10.1002/qj.49711146709

Houghton, D. D., & Kasahara, A. (1968). Nonlinear shallow fluid flow over an isolated ridge. Communications on Pure and Applied Mathematics, 21(1), 1-23. https://doi.org/10.1002/cpa.3160210103

Howard, L. N. (1961). Note on a paper of John W. Miles. Journal of Fluid Mechanics, 10(4), 509-512. https://doi.org/10.1017/S0022112061000317

Jang, W., & Chun, H.-Y. (2008). Severe Downslope Windstorms of Gangneung in the Springtime. Atmosphere, 18(3), 207-224. (In Korean with English Abstract)

Jang, W., & Chun, H.-Y. (2010). A numerical study on severe downslope windstorms occurred on 5 April 2005 at Gangneung and Yangyang, Korea. Asia-Pacific Journal of Atmospheric Sciences, 46(2), 155-172. https://doi.org/10.1007/s13143-010-0015-2

Jo, E., Park, C., Son, S. W., Roh, J. W., Lee, G. W., & Lee, Y. H. (2020). Classification of localized heavy rainfall events in South Korea. Asia-Pacific Journal of Atmospheric Sciences, 56(1), 77-88. https://doi.org/10.1007/s13143-019-00128-7

Kim, J., & Paik, K. (2015). Recent recovery of surface wind speed after decadal decrease: a focus on South Korea. Climate Dynamics, 45(5), 1699-1712. 10.1007/s00382-015-2546-9

Kim, J. H., & Chun, H. Y. (2010). A numerical study of clear-air turbulence (CAT) encounters over South Korea on 2 April 2007. Journal of applied meteorology and climatology, 49(12), 2381-2403. https://doi.org/10.1175/2010JAMC2449.1

Kim, J.-H., & Chung, I.-U. (2006). Study on Mechanisms and Orographic Effect for the Springtime Downslope Windstorm over the Yeongdong Region. Atmosphere, 16(2), 67-83. (In Korean with English Abstract)

Kiviluoto, K. (1996, June). Topology preservation in self-organizing maps. In Proceedings of International Conference on Neural Networks (ICNN'96) (Vol. 1, pp. 294-299). IEEE. 10.1109/ICNN.1996.548907

Klemp, J. B., & Lilly, D. R. (1975). The dynamics of wave-induced downslope winds. Journal of Atmospheric Sciences, 32(2), 320-339. https://doi.org/10.1175/1520-0469(1975)032<0320:TDOWID>2.0.CO;2

Kohonen, T. (1995). Self-organizing maps.

Kohonen, T. (2013). Essentials of the self-organizing map. Neural networks, 37, 52-65. https://doi.org/10.1016/j.neunet.2012.09.018

Lee, J., Seo, J. M., Baik, J. J., Park, S. B., & Han, B. S. (2020). A Numerical Study of Windstorms in the Lee of the Taebaek Mountains, South Korea: Characteristics and Generation Mechanisms. Atmosphere, 11(4), 431. https://doi.org/10.3390/atmos11040431

Lee, J. G., & In, S. R. (2009). A numerical sensitivity experiment of the downslope windstorm over the Yeongdong region in relation to the inversion layer of temperature. Atmosphere, 19(4), 331-344.

Lilly, D. K. (1978). A severe downslope windstorm and aircraft turbulence event induced by a mountain wave. Journal of Atmospheric Sciences, 35(1), 59-77. https://doi.org/10.1175/1520-0469(1978)035<0059:ASDWAA>2.0.CO;2

Lin, Y. L., & Wang, T. A. (1996). Flow regimes and transient dynamics of two-dimensional stratified flow over an isolated mountain ridge. Journal of the atmospheric sciences, 53(1), 139-158. https://doi.org/10.1175/1520-0469(1996)053<0139:FRATDO>2.0.CO;2

Liu, Y., Weisberg, R. H., & Mooers, C. N. (2006). Performance evaluation of the self-organizing map for feature extraction. Journal of Geophysical Research: Oceans, 111(C5). https://doi.org/10.1029/2005JC003117

Loikith, P. C., Lintner, B. R., & Sweeney, A. (2017). Characterizing large-scale meteorological patterns and associated temperature and precipitation extremes over the northwestern United States using self-organizing maps. Journal of Climate, 30(8), 2829-2847. https://doi.org/10.1175/JCLI-D-16-0670.1

Long, R. R. (1953). Some aspects of the flow of stratified fluids: I. A theoretical investigation. Tellus, 5(1), 42-58. https://doi.org/10.3402/tellusa.v5i1.8563

Long, R. R. (1954). Some aspects of the flow of stratified fluids: II. Experiments with a two-fluid system. Tellus, 6(2), 97-115. https://doi.org/10.1111/j.2153-3490.1954.tb01100.x

Miles, J. W. (1961). On the stability of heterogeneous shear flows. Journal of Fluid Mechanics, 10(4), 496-508. https://doi.org/10.1017/S0022112061000305

Miles, J. (1986). Richardson's criterion for the stability of stratified shear flow. The Physics of fluids, 29(10), 3470-3471. https://doi.org/10.1063/1.865812

Neal, R., Fereday, D., Crocker, R., & Comer, R. E. (2016). A flexible approach to defining weather patterns and their application in weather forecasting over Europe. Meteorological Applications, 23(3), 389-400. https://doi.org/10.1002/met.1563

Nguyen-Le, D., & Yamada, T. J. (2019). Using weather pattern recognition to classify and predict summertime heavy rainfall occurrence over the Upper Nan river basin, northwestern Thailand. Weather and Forecasting, 34(2), 345-360. https://doi.org/10.1175/WAF-D-18-0122.1

Ohba, M., Kadokura, S., Yoshida, Y., Nohara, D., & Toyoda, Y. (2015). Anomalous weather patterns in relation to heavy precipitation events in Japan during the Baiu season. Journal of Hydrometeorology, 16(2), 688-701. https://doi.org/10.1175/JHM-D-14-0124.1

Philipp, A., Della-Marta, P. M., Jacobeit, J., Fereday, D. R., Jones, P. D., Moberg, A., & Wanner, H. (2007). Long-term variability of daily North Atlantic–European pressure patterns since 1850 classified by simulated annealing clustering. Journal of Climate, 20(16), 4065-4095. https://doi.org/10.1175/JCLI4175.1

Scorer, R. S. (1949). Theory of waves in the lee of mountains. Quarterly Journal of the Royal Meteorological Society, 75(323), 41-56. https://doi.org/10.1002/qj.49707532308

Seluchi, M. E., Norte, F. A., Satyamurty, P., & Chou, S. C. (2003). Analysis of three situations of the foehn effect over the Andes (zonda wind) using the Eta–CPTEC regional model. Weather and forecasting, 18(3), 481-501. https://doi.org/10.1175/1520-0434(2003)18<481:AOTSOT>2.0.CO;2

Vautard, R., Cattiaux, J., Yiou, P., Thépaut, J. N., & Ciais, P. (2010). Northern Hemisphere atmospheric stilling partly attributed to an increase in surface roughness. Nature geoscience, 3(11), 756-761. 10.1038/NGEO979

Vosper, S. B. (2004). Inversion effects on mountain lee waves. Quarterly Journal of the Royal Meteorological Society: A journal of the atmospheric sciences, applied meteorology and physical oceanography, 130(600), 1723-1748. https://doi.org/10.1256/qj.03.63

Wang, T. A., & Lin, Y. L. (2000). Effects of shear and sharp gradients in static stability on two-dimensional flow over an isolated mountain ridge. Meteorology and Atmospheric Physics, 75(1), 69-99. https://doi.org/10.1007/s007030070017

Zeng, Z., Ziegler, A. D., Searchinger, T., Yang, L., Chen, A., Ju, K., ... & Wood, E. F. (2019). A reversal in global terrestrial stilling and its implications for wind energy production. Nature Climate Change, 9(12), 979-985. https://doi.org/10.1038/s41558-019-0622-6